AUTHOR(S):

Kubo, Kiyoshi

MEASUREMENT OF SHAPE PARAMETERS FOR MULTIHADRONIC EVENTS IN ELECTRON ANNIHILATION AT $\sqrt{S}=52$ GeV.

By

Kiyoshi KUBO*

Department of Physics, Faculty of Science, Kyoto University

(*Received July 29, 1988*)

Abstract

The multihadronic production in the electron-positron interaction, $e^+e^- \to$ hadrons, has been studied at the center-of-mass energy of 52 GeV by the VENUS detector at TRISTAN (KEK). For the integrated luminosity of 2.9 pb^{-1}, 399 multihadronic events were collected. By selecting 300 events with good qualities from these 399 events, the shape analysis was performed to search for the signature of the open t-quark production.

The results are consistent with the five known quark hypothesis and there is no evidence for the t-quark production. The quantitative analysis for the acoplanarity distribution concludes that the upper limit of the cross section of the open t-quark production is 17 pb at the 95% confidence level.

1. Introduction

The Weinberg-Salam theory has been established as the standard theory of elementary particles concerning the electromagnetic and weak interactions. Almost all experimental observations are consistent with this theory.

Among the members of the particles predicted in the theory, the Higgs particle and the top-quark have not been discovered. The investigation of the top-quark (t) is of great importance, since the t-quark is expected to complete three SU (2) doublets of the weak interaction together with the well confirmed five known quarks of u, d, s, c and b-quark according to the Kobayashi-Maskawa theory.[1-1] The existence of the t-quark will give us the natural explanation of the CP violation observed in the decay of neutral K meson.

The c and b-quarks were found in hadron interactions and also in electron positron collisions.[1-2] Proton anti-proton colliding machines have achieved higher beam energies than electron positron colliders. However, the quarks in the proton or anti-proton share only a fraction of the beam momentum, as a result the effective energy of the quark-anti-quark interaction is not unique. Besides, a number of hadrons produced from the non-interacting quarks make the event analysis complicated.

A few experimental evidences of the t-quark production in the proton anti-proton collision at CERN were reported.[1-3] However these results have not been

---

* Now at the National Laboratory for High Energy Physics (KEK), Tsukuba 305, Japan.

confirmed finally, because the clean separation of t-quark signatures from the backgrounds was failed after the accumulation of more data.

On the other hand, in the case of electron positron collider, electrons and positrons have no structure, so that the effective energy for the new quark production is defined exactly by the beam energy. The multiplicity of hadron production is also smaller than that in the hadron collision. Therefore, the study of e^+e^- collision is easier to observe the signature of t-quark production than the hadron collision.

The existence of the t-quark can be studied by measuring the total cross section of e^+e^- annihilation into hadrons. The R-ratio is defined as the ratio of the total hadronic cross section to the cross section of $e^+e^- \rightarrow \mu^+\mu^-$ reaction in the lowest order QED. According to the naive quark-parton model, the R-ratio can be expressed as follows:

$$R(QED) = 3 \sum_f Q_f^2, \tag{1.1}$$

where f is a flavour index, Q_f is the charge of the flavour and 3 is the color factor. If the beam energy is lower than the t-quark (charge 2/3) mass, the $R(QED)$ is expected to be 11/3. On the other hand, when the beam energy exceeds the t-quark mass, a pair of the 'open' t-quark and anti t-quark pair will be produced. In consequence, the $R(QED)$ will increase from 11/3 to 15/3. Here, the 'open' t-quark means the t-quark which is bound with other light quark and can be observed as a meson. This meson is called as the 'topped meson'. The R-ratio has been measured at PETRA (DESY) and PEP(SLAC) up to the beam energy of 23.4 GeV[1-4][1-5] and it has been found that there is no increase of the R-ratio suggesting the production of the 'open' t-quark and anti-t-quark. Of course, the existence of the $t\bar{t}$ bound state can be observed as a sharp peak of the total hadronic cross section. However, the widths of the resonance states are expected to be extremely narrow, so that the search for the resonance states is expected to be difficult.

The shape of hadronic events with the new quark production is expected to be distinguishable from ordinary hadronic events. When the beam energy is just above the t-quark mass, the produced t-quark moves with a low velocity. The angular distribution of the decayed particles, therefore, tends to be broad, and the event shape is expected to be spherical. On the other hand, the angular distribution of the final particles from the production of a light quark pair tends to be narrow, because the produced quark and anti-quark having the high momenta move opposite each other in their cm system, and then they are observed as the two jets through the fragmentation and decay processes. The resonance state of $t\bar{t}$ will show a different event shape from the 'open' $t\bar{t}$ production. The shape in this case is expected to be rather similar to that of the light quark production. Therefore, the high sensitivity for open t-quark search can be achieved by studying the shape of hadronic events. The shape of hadronic events has been also studied at PETRA[1-4] up to the beam energy of 23.4 GeV. It was found that the shape agrees with that expected from the prediction by the Monte Carlo simulation with five known quarks.

The MARK-J group observed spherical hadronic events which accompanied isolated muons at the highest beam energy of PETRA ($\sqrt{s}$ =46.3—46.78 GeV)[1-5]. The number of such events is significantly larger than the expected value from the ordinary processes. This may be a signal of new particle production; the t-quark is one of the candidates. The JADE group made the same analysis, and also observed an excess of spherical hadronic events with isolated muons.[1-6] On the other hand, the CELLO group did not observed such anomalies.[1-7] All the groups did not found any excess of spherical hadronic events with isolated electrons. The experiment at higher beam energies has been eagerly waited for to give the conclusion to this interesting problem.

TRISTAN at KEK started to collide the electron and positron beams at 24 GeV on November 1986 and then at 25 GeV on Jan. 1987. From June 26 to July 25, 1987, TRISTAN was successfully operated at the beam energy of 26 GeV. The integrated luminosity reached to 0.7 pb^{-1} at 25 GeV and 2.9 pb^{-1} at 26 GeV at the VENUS detector.

This paper reports the results on the search for the 'open' t-quark by studying the shape of multihadronic events.

2. Experimental apparatus

2.1. General

TRISTAN is the electron-positron colliding accelerator ring of the world highest energy constructed at KEK (National Laboratory for High Energy Physics) in Tsukuba Science City, Japan. The details are given in Ref. (2–1).

TRISTAN came into operation at the beam energy of 25 GeV since January 1987. Then the beam energy was increased to 26 GeV in June 1987. The designed beam energy is 35 GeV, and this maximum energy is scheduled to be achieved in the summer of 1989 by installing superconducting RF cavities.

The luminosity of electron positron collision is given as follows:

$$L = \frac{I_+ I_-}{f_{rev} N_b e^2 4\sigma_x \sigma_y}, \qquad (2.1)$$

where I_- and I_+ are the beam currents of positrons and electrons, respectively. f_{rev} is the revolution frequency. N_b is the number of bunches. e is the charge of electron. σ_x and σ_y denote the r.m.s. of the beam sizes at the colliding point in the horizontal and vertical directions, respectively. The data for 26 GeV were collected consuming the machine time of 530 hours spreading over June to July 1987. The peak luminosity of 6×10^{30} cm^{-2} sec^{-1} was achieved and the average luminosity was about 10^{30} cm^{-2} sec^{-1} at the beam energy of 26 GeV. The total number of triggered events amounted to 4.6×10^6.

2.2. VENUS detector[2-2]

The VENUS detector is placed in the FUJI experimental hall at the south west

straight section of the main ring of TRISTAN.   The design principles of the VENUS detector are; (1) to work as a general purpose detector covering almost whole solid angle of 4π, (2) to use well established technique so as to be constructed within the scheduled date, and (3) to reserve a space inside the magnet for future upgrading.

A view of the VENUS detector is shown in Fig. 1.   The direction of the electron beam at the colliding point is defined to be the z direction in our standard coordinate system.   The x and y directions are defined as the outward direction from the center of the main ring and the vertical upper direction, respectively.

The central drift chamber (CDC)[2-3], the inner chamber (IC)[2-4] (details are given in Appendix II), the outer drift tubes (ODT) and time of flight counters (TOF) [2-5] are used to detect charged particles.   The superconducting solenoid magnet[2-6] covers the wire chambers such as CDC, IC and ODT to measure the momentum of charged particles.   The lead glass calorimeter (LG)[2-7], luminosity monitor (LM)[2-8] and liquid argon calorimeter (LA) are provided to detect electrons and photons.   The barrel streamer tubes (BST)[2-9] are placed between LG and the solenoid magnet to measure the position of photons converted in the coil.   The muon chambers (MU)[2-10] are placed in the outermost region.   Open spaces between CDC and ODT, and between CDC and LA are reserved for future installations of upgraded detectors.

CDC is of a cylindrical shape and 3 m in length.   The inner and outer radii are 0.25 m and 1.25 m, respectively.   It has 7104 sense wires and 21312 field wires. There are two kind of sense wires.   The first kind of wires are the axial wires which are parallel to the z axis.   These axial wires are used to measure the positions on the x–y plane.   Signals from the axial wires in the inner 14 layers are used for triggering.
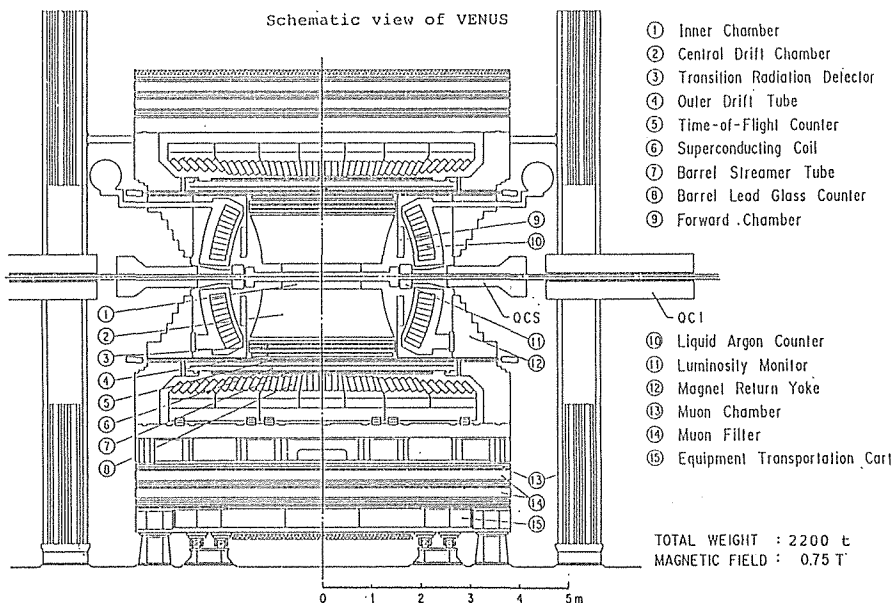

Schematic view of VENUS

① Inner Chamber
② Central Drift Chamber
③ Transition Radiation Detector
④ Outer Drift Tube
⑤ Time-of-Flight Counter
⑥ Superconducting Coil
⑦ Barrel Streamer Tube
⑧ Barrel Lead Glass Counter
⑨ Forward .Chamber

⑩ Liquid Argon Counter
⑪ Luminosity Monitor
⑫ Magnet Return Yoke
⑬ Muon Chamber
⑭ Muon Filter
⑮ Equipment Transportation Cart

TOTAL WEIGHT : 2200 t
MAGNETIC FIELD : 0.75 T

Fig. 1.   Side view of the VENUS detector.

The other kind of wires are the stereo wires, which have an angle of 3.5° with respect to the beam axis. They are used to measure positions in the z-axis. The number of layers of the axial wires and the stereo wires are 20 and 9, respectively.

The spacial resolution of each wire in the x–y plane is 440 μm in the stage of the present experiment. The resolution in the z-direction is 10 mm. The momentum resolution obtained from the Bhabha events with the magnetic field of 0.75 Tesla is expressed as

$$\Delta p_t / p_t = 0.015 \times p_t , \tag{2.2}$$

where p_t is the transverse momentum in GeV/c.

The TOF counters are cylindrically placed on the inside wall of the solenoid magnetic coil. The radius of the counter system is 1.66 m from the beam axis. TOF consists of 96 plastic scintillation counters of 466 cm long, 4.2 cm thick and 10.8 cm wide. Each counter is viewed by two photomultiplier tubes at both ends[2-5].

The time resolution obtained by the preliminary analysis is less than 500 psec. In the present experiment, TOF was used to trigger the events with coplaner tracks.

LG consists of 5160 lead glass blocks of DF6, and is segmented into 120 in the φ direction and into 43 in the z direction. It covers the polar angles from 37° to 143° and the whole azimuthal angle of 4π.

The cross section of one block is 12 cm × 11 cm and the length is 30 cm, which corresponds to 18 radiation lengths. The energy resolution of the calorimeter for electrons was evaluated by using the Bhabha events and low multiplicity electron events which mainly come from the $e^+e^- \rightarrow e^+e^-e^+e^-$ reaction. The results are

$$\Delta E = 0.054 \times \sqrt{E} + 0.028 \times E , \tag{2.3}$$

where E is the energy of electrons in GeV.

The lead glass blocks are divided into seven rings in the z-direction, and each rings except the central ring are divided into eight in the φ direction. The central ring is divided into ten. As the results, the lead glass blocks are grouped into 58. The analog signals are summed in each group. When the pulse height of this analog sum signal is greater than a preset threshold, a trigger signal is generated and is called as the 'segment energy sum' signal. The 'total energy sum' signal is generated if the sum of signals from the all calorimeter blocks is greater than a threshold.

LM was used to detect small angle electrons and photons mainly from the Bhabha and two photon interactions, and consists of two parts. They are placed around the beam pipe at both end cap regions.

The angular coverage of the calorimeter is from 40 to 140 mradian in the polar angle. Each carolimeter is a sandwich type of lead and plastic scintillator having the total thickness of 19 radiation lengths.

The electron and positron beams cross every 5 μs at the center of straight section. The trigger system supplies a signal to the host computer of VAX11/780 if it decides to take the data in the present beam crossing.
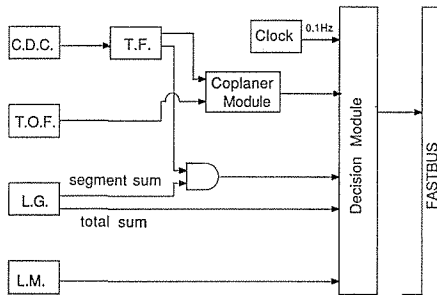
Fig. 2.   Diagram of the trigger system.

The diagram of the trigger system is shown in Fig. 2.   The track finder (TF) receives the hit pattern of CDC axial wires in the 1st layer to the 14th layer, and finds tracks having high transverse momentum and originating from near the beam axis. TF has 64 divisions in the φ direction, which corresponds to the angular resolution of 5.6°.   The trigger system also receives the hit pattern of the TOF counters.   If the TOF counters have a hit which corresponds to the track found by TF, this track is called as 'TOF associated track'.

The track finding efficiency is evaluated by the Monte Carlo simulation.   The efficiency is found to be almost 100% for the tracks having the transverse momentum of larger than 0.7 GeV/c and the polar angles from 30° to 150°.   For 'TOF associated tracks', however, there is the inefficiency of about 3% due to the gaps between the TOF counters.

The trigger system receives 'total energy sum' and 'segment energy sum' signals from the lead glass calorimeter, as will be described in the following section.   The trigger system also receives the hit information of the luminosity monitor.

Using these information, the trigger system decides whether the event should be taken or not.

Data from the detectors are taken by the VAX–11/780 computer through the FASTBUS system in the readout time of typically 25 msec, then they are sent to a FACOM-382 computer through a 1 km long optical fiber cable and stored on cassette magnetic tapes[2-11].   The data size is about 5k bytes per event.   The VAX-11 also monitors the conditions of the beam, detectors and electronics, and displays sampled events on real time.

3.   Trigger condition

In this experiment the following five kinds of triggers were used.

(1)   Total energy sum trigger; the total energy sum signal from the lead glass calorimeter with the threshold of 5 GeV.

(2)   Segment energy sum trigger; at least one segment sum signal from the lead glass calorimeter with the threshold of 0.5 GeV, and at least two CDC tracks identified by the track finder (TF).

(3)   Coplaner track trigger; at least one pair of 'TOF associated' back-to-back tracks within an acoplanarity angle of 11.1°.

(4) Luminosity monitor trigger; at least one pair of back-to-back particles detected by LM with the energy deposit greater than 18 GeV for each particle.

(5) No biased trigger; a random trigger which synchronized to the beam crossing with the rate of 0.1 Hz.

The trigger (1), (2) and (3) are provided mainly to detect the multihadronic events, large angle Bhabha events etc., while the trigger (4) is provided to detect the small angle Bhabha event. The trigger (5) is for studying the beam conditions and for monitoring the performances of the detectors and the data taking processes. The typical trigger rate was about 6 Hz just after the beam filling and about 4 Hz on an average. The dead time due to the data acquisition was about 20% at the maximum and 10% on an average.

4. Monte Carlo simulation

The Monte Carlo simulation was performed to evaluate the acceptance of the VENUS detector. The simulation program consists of two parts. The first part is called as 'Event Generator' which simulates the production of particles. The second part simulates the detector responses for all the particles in the events generated by 'Event Generator', including the interactions with materials and decays in the detector.

4.1. Event generator

(A) Multihadronic event generator

Three kinds of Monte Carlo models were used for the simulations of multihadronic production. The LUND Monte Carlo (version 5.3)[4-1] was mainly used in this analysis, because this model has been used widely and is well established. Its parameters have been well studied at PETRA and PEP energies.[4-2,3]

The predictions of the LUND version 6.3[4-4] and the WEBBER[4-5] models were compared with the result of the present experiment and these of the LUND 5.3 model. There are some differences between these models on the observables such as the thrust, acoplanarity and sphericity. These differences are treated as systematic errors.

The event generator can be divided into two steps. The first step is the generation of partons (quarks and gluons). In the LUND 5.3 model, this process is calculated according to the e^+e^- annihilation including the weak neutral current and the second order QCD effect. Combinations of partons such as $q\bar{q}$, $q\bar{q}g$, $q\bar{q}q\bar{q}$, $q\bar{q}gg$ are generated as shown in Fig. 3. The radiative corrections such as shown in Fig. 4 are included in this calculation. They are the initial state radiation, the vacuum polarization effect and the initial state vertex correction. The calculations were given by Berends, Kleiss and Jadach.[4-6] In the LUND 6.3 and the WEBBER models, the parton shower model is used in this parton generation step. Parton showers are produced according to the leading log approximation of QCD as schematically shown in Fig. 5. The weak neutral current and radiative corrections are also taken into account.

In the second step of the event generator, multihadrons (color singlet) are produced from the colored partons through the fragmentation process. If quarks or
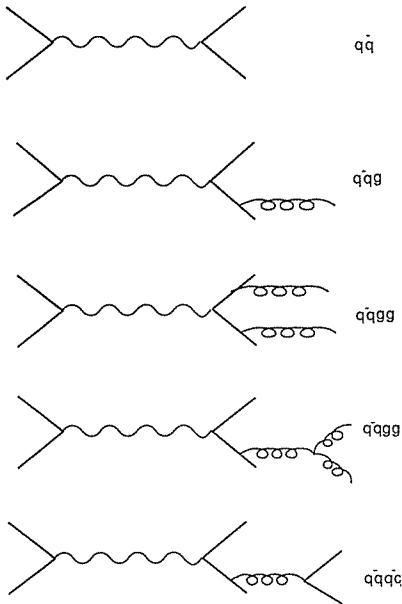
Fig. 3. Tree level diagrams for the hadronic event up to 2nd order QCD in the LUND 5.3 model.
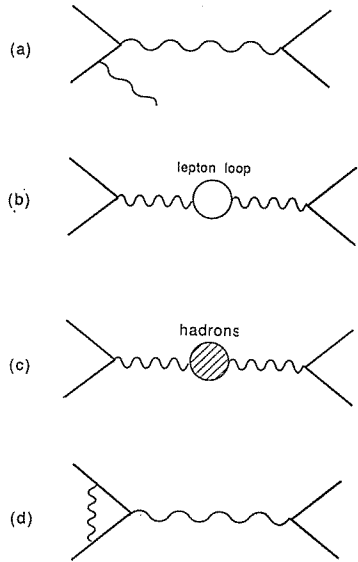

Fig. 4. Feynman diagrams of radiative cor-rction, (a) initial state radiation, (b) vacuum polarization with lepton loop, (c) vacuum polarization with hadronic state and (d) vertex correc-tion.
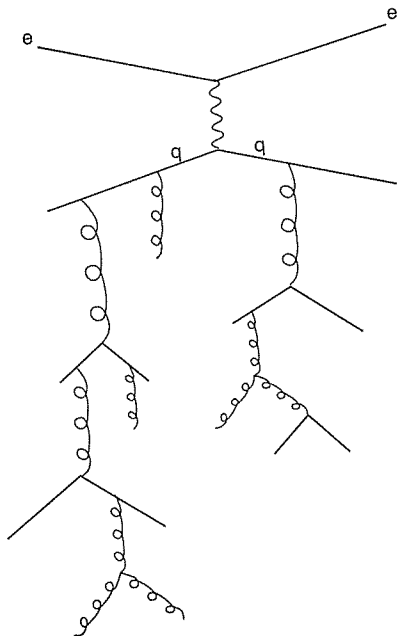

Fig. 5. Example of parton showers in the LUND 6.3 and WEBBER models.

gluons are created as their daughters, then the fragmentation step begins again for each parton. The decay of produced hadrons are simulated if they are unstable particles. The LUND 5.3 and LUND 6.3 models are based on the string model in the fragmentation process. In the WEBBER model, on the other hand, the cluster type model is chosen.

The fragmentation function in the LUND 5.3 model is given as follows[4-1]:

$$f(z) = z^{-1}(1-z)^a \exp\left(-bm_T/z\right),\tag{4.1}$$

with

$$z = \frac{E_1 + P_{//1}}{E_2 + P_{//2}}, \quad m_T^2 = m^2 + \sigma_{pt}^2,\tag{4.2}$$

where E_1 and E_2 are the energies of parent quark and daughter hadron, respectively. $P_{//1}$ and $P_{//2}$ are the momenta of parent quark and daughter hadron, respectively, parallel to the most ancient partons in the event. m is the mass of the daughter hadron. The parameters used in the fragmentation are a, b and σ_{pt}. The longitudinal momenta of hadrons are determined by mainly the parameter a. The transverse momenta are determined by mainly b and σ_{pt}. Y_{min} is another parameter in the parton generation,[4-1] and it corresponds to the lower limit of the scaled invariant mass of two partons in three parton or four parton events. The values of these parameters are chosen so as to reproduce the experimental results at PEP and PETRA[4-2,3].

These values are

$$a = 1.0,$$
$$b = 0.63,$$
$$\sigma_{pt} = 0.37,$$
$$Y_{min} = 0.02.$$

By changing these parameters within reasonable regions, the systematic error of the detection efficiency was evaluated as will be discussed in Section 5.4 (E).

The parameters for the LUND 6.3 and the WEBBER models were chosen according to Ref. (4–7). The results from these Monte Carlo simulations must be normalized by the total cross section of multihadron production predicted by the electro-weak theory and QCD to compare with the experimental results. The details on the calculation of the cross section is given in Appendix 1. The total cross section with five known quarks at $\sqrt{s} = 52$ GeV is calculated to be

$$\sigma_{total} = 143 \text{ pb}.\tag{4.3}$$

This gives the following R value as the theoretical prediction,

$$R = 4.43.\tag{4.4}$$

As was mentioned before, the Monte Carlo simulation includes the radiative

corrections, so that the effect of radiative corrections must be taken into account for this total cross section. The fraction of the radiative corrections is calculated to be 0.31 at $\sqrt{s}=52$ GeV according to the method by Berends, Kleiss and Jadach[4-6]. Finallly the total cross section including radiative corrections is calculated to be

$$\sigma_{total}(1+\delta) = 143\ (1+0.31) = 187\ \text{pb}\ . \tag{4.5}$$

(B) 'Open' t-quark generator

The production of the t-quark is simulated using the LUND 5.3 and LUND 6.3 models. The parton generation scheme, the fragmentation scheme and the values of parameters are the same as those in the five known quark productions. The t-quark is assumed to decay into the b-quark and virtual W-boson ($t \rightarrow b+W^*$). The branching ratio of W^* is assumed to be as follows:

$$t \rightarrow b+u+d \quad 37\%$$
$$t \rightarrow b+c+s \quad 29\%$$
$$t \rightarrow b+e+\nu_e \quad 12\%$$
$$t \rightarrow b+\mu+\nu_\mu \quad 12\%$$
$$t \rightarrow b+\tau+\nu_\tau \quad 10\%$$

The cross section of open t-quark production will be discussed in Section 5.4 (F).

(C) Two photon process

The two photon event ($e^+e^- \rightarrow e^+e^- + hadrons$) can be mis-identified as the multi-hadronic event in our VENUS detector, and is contaminated as the background. Two kinds of event generators were provided. One is based on the generalized vector dominance model (GVDM) and the other is the quark parton model (QPM). In QPM processes, u, d, s, c and b-quarks are produced separately. The fragmentation process of these event generators is the same as that of the LUND 5.3 or 6.3 models.

(D) Tau pair production

The tau pair production is also regarded as the background. The effects of the first-order weak neutral current and the radiative correction are taken into account to generate the events. The fragmentation process is based on the LUND models.

4.2. Detector simulation

The behaviors of the particles generated by the event generator are simulated in the detector. This simulation is performed with every short step along the particle path. The interaction of the particle with the detector material and the decay of the particle are treated statistically in each step. Then, the responses of all the detector components such as the hits in CDC, the pulse heights of the lead glass counters and so on are evaluated. These responses are digitized with the same format as that of the real data. The position and energy resolutions of each detector component are taken into account in this digitization process. Then the simulated events are analysed using exactly the same program as that for the real events. This simulation program is named as 'VMONT' (VENUS Monte Carlo).

5. Analysis

5.1. Tracking and clustering

In order to analyze the measured events, it is necessary to reconstruct the trajectories of the charged particles measured by CDC, and to calculate the energy deposits in the lead glass calorimeter.

The most of the reconstruction of tracks was performed using the computer tracking program with the full algorithm, which was developed by Nakagawa *et al.*[5-1] In the first step of the event selection, a shortened algorithm is used to reduce the computer CPU time (see Section 5.3). The shortened algorithm does not try to find the tracks of which radii are less than 80 cm in the initial roading. The shortened algorithm performs the track fitting routine only once, while the full algorithm iterates it three times.

The efficiency of the track reconstruction was estimated for both observed events and Monte Carlo simulated events. The efficiency is found to be almost 100% for the Bhabha events with the polar angle from 25° to 155°. The efficiency for the simulated Bhabha events coincided with that for the observed events. For the multihadronic events, on the other hand, the efficiency amounted to 90% on an average for the same region of the polar angle because there are some tracks which can not be separated from other tracks.

In order to measure the energy deposit and the hit position on the lead glass calorimeter, a computer clustering program is developed. Fired lead glass blocks are grouped every shower cluster. Then the hit position was calculated with the energy weighted average method. The θ and φ angles of the hit position were calculated from the following expressions.

$$\theta = \frac{\sum_i \theta_i E_i^a}{\sum_i E_i^a}, \tag{5.1}$$

$$\varphi = \frac{\sum_i \varphi_i E_i^a}{\sum_i E_i^a}, \tag{5.2}$$

where i runs through all lead glass blocks in the cluster. θ_i and φ_i are the polar and azimuthal angles of the center of mass of the i-th lead glass block, respectively. E_i is the energy deposit in the i-th lead glass block. a is a weighting parameter, and is chosen to be 0.34.

5.2. Integrated luminosity

The integrated luminosity is evaluated from the number of large angle Bhabha events measured with the lead glass calorimeter[5-2]. The Bhabha events were selected by the following criteria.

(a) There are at least two high energy shower clusters, each of which has the energy higher than one third of the beam energy.

(b) At least one pair of above clusters are collinear with the allowance of 10°.

(c)   Both clusters in the above pair are in the fiducial volume; $|\cos\theta_{cluster}| \leqq$ 0.743, or $42° \leqq \theta_{cluster} \leqq 138°$.

(d)   Both clusters in the pair are associated with the 'good tracks'. The angle between the center of the shower and the track hit point on the surface of the lead glass block coincides within 5°. 'Good track' means the track which is well reconstructed and satisfies the conditions described in Section 5.3 (A).

(e)   The number of 'good tracks' in the event is less than or equal to 6.

Out of 4.6 millions of triggerd events, 1195 events remained after the above selection.

The integrated luminosity can be calculated by

$$\int Ldt = N \times \sigma \times f, \tag{5.3}$$

where N is the observed number of events, σ is the integrated cross section of Bhabha scattering over our acceptance, and f is the correction factor due to the imperfection of our acceptance calculation as will be mentioned below.

The integrated cross section of Bhabha scattering of the lowest order QED for the polar angles from 42° to 138° was calculated to be

$$\sigma_{ee\,QED}(42° \leqq \theta \leqq 138°) = 0.435 \text{ nb} . \tag{5.4}$$

Taking into account the effect of the weak interaction, the radiative correction up to the order of α^3 and the selection criteria, the cross section σ in Eq. (5.3) is evaluated to be

$$\sigma = 0.411 \text{ nb.} \tag{5.5}$$

There were about 20 dead blocks in the lead glass calorimeter. The spacial resolution of hit position in the calorimeter is finite. These defects must be taken into account in the evaluation of the integrated luminosity. The correction factor is calculated to be as follows:

$$f = 0.996 . \tag{5.6}$$

Finally, the integrated luminosity amounted to

$$\int Ldt = 2.90 \pm 0.08 \pm 0.11 \text{ pb}^{-1} . \tag{5.7}$$

The first and second errors are the statistical and the systematic errors, respectively. The systematic error of 4% comes from uncertainties on the following quantities: the probability of bremsstrahlung, the uncertainties of the correction factor for the dead blocks, the cluster position calculation, and the setting of the detectors.

5.3.   Event selection for multihadronic event

(A)   Preselection

At first, all the energy deposits in the lead glass calorimeter were summed up.

This sum is called as the 'total barrel energy (E_{LG})'. Then the events which had the total barrel energy larger than 3 GeV and at least two accepted tracks were selected. Here the tracking program with the shortened algolithm was used to save a computer CPU time. In this algolithm, an 'accepted track' must satisfy the following requirements:

    (a)   Track can be reconstructed in three dimensions.

    (b) $N_{hit-xy} \geq 8$ and $N_{hit-rz} \geq 4$, where N_{hit-xy} is the number of hits on axial wires and N_{hit-rz} is the number of hits on stereo wires of CDC.

    (c) $d_{r0} < 3$ cm and $|d_{z0}| < 30$ cm, where d_{r0} is the radius and d_{z0} is the z-co-ordinate at the closest approach to the beam axis.

    (d)   Transverse momentum is larger than 0.2 GeV/c.

For the events which remained after the above selection, the track reconstruction was done again with the full tracking algolithm. Then the events with at least 5 'good tracks' were selected.

The requirements for the 'good track' in this time are as follows:

    (a')   Track reconstructed in three dimensions.

    (b') $N_{hit-xy} \geq 8$ and $N_{hit-rz} \geq 4$.

    (c') $d_{r0} < 2$ cm and $|d_{z0}| < 20$ cm.

    (d')   Transverse momentum is larger than 0.2 GeV/c.

These requirements (a')–(d') are the same as the requirements (a)–(d) except the requirement (c') which is tighter than (c). Because the reconstruction efficiency of the shortened algolithm is less than that of the full algolithm, the condition of the previous track selection (at least two 'accepted tracks') was chosen to be loose enough so that the probability of rejecting the events which have at least 5 'good tracks' is negligibly small.

Out of 4.6 millions of triggered events, 673 events remained after this selection.

    (B)   Selection of multihadronic events

The following selection was further applied to the events selected by the preselection: the total visible energy is greater than the beam energy, $E_{vis} \geq E_{becm}$. E_{vis} is defined as

$$E_{vis} = \sum_j |\vec{p}_j| + \sum_i E_i , \qquad\qquad (5.8)$$

where $\vec{p}$ denotes the track momentum and E is the shower cluster energy. An index i runs through all shower clusters of the lead glass calorimeter. An index j run through tracks which satisfy the following requirements:

    (a)   Track reconstructed in three dimensions

    (b) $N_{hit-xy} \geq 8$ and $N_{hit-rz} \geq 4$.

    (c) $d_{r0} < 3$ cm and $|d_{z0}| < 30$ cm.

Finally, 399 events were selected as the multihadronic events. Figs. 6 and 7 show the E_{LG} distribution and the N_{good} distribution for the final multihadronic events, respectively. The histogram in each figure represents the distribution for the Monte Carlo events (LUND 5.3). These figures show that the cut value of 3.0 GeV
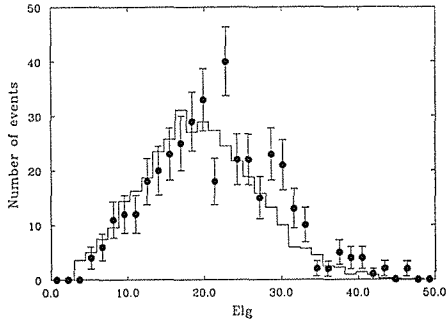
Fig. 6. Distributions of the total energy in the lead glass calorimeter for the final multihadronic events (closed circle) and for the Monte Carlo events (histogram).
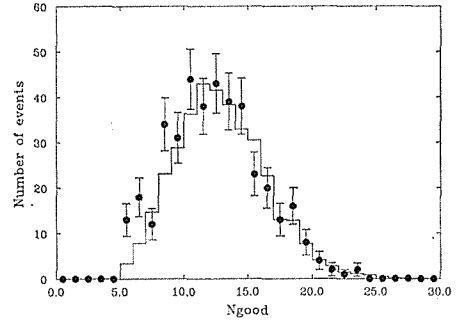

Fig. 7. Distributions of the number of 'good tracks' for final multihadronic events (closed circle) and for the Monte Carlo events (histogram).
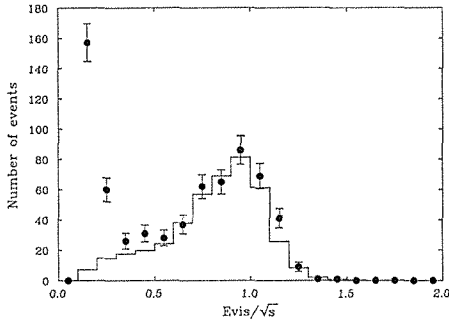

Fig. 8. Distributions of the visible energy normalized by $\sqrt{s}$ for the preselected events (closed circle) and for the Monte Carlo events (histogram).

for E_{LG} and 5 for N_{good} in the preselection are not critical for the multihadronic events. Fig. 8 shows the $E_{vis}/\sqrt{s}$ distribution of the preselected events. The histogram in the figure represents the distribution of the Monte Carlo events (LUND 5.3).

As will be described in Section 5.3 (E), the Monte Carlo simulation shows that the events with the low visible energy come mainly from the two photon interaction of $e^+e^- \rightarrow e^+e^-$ +hadrons.

(C)   Trigger inefficiency

As was described in Chapter 3, there are three triggers relevant to the multi-hadronic events. There are the total energy trigger (1), segment energy sum trigger (2) and coplaner track trigger (3).

Out of 399 events selected as the multihadronic event, the number of events associated with the above three trigger conditions are as follows:

(1)   Total energy trigger   399,
(2)   Segment energy sum trigger   399,
(3)   Coplaner track trigger   389.

The number of events from the total energy trigger is different from that of the coplaner track trigger. The total energy trigger is generated from LG, while the coplaner track trigger is generated from CDC and TOF. These two triggers are

independent each other.   Therefore, the trigger inefficiency, which is the probability that the both triggers miss the multihadronic event, can be evaluated from these numbers as follows.

389 events of the coplaner track trigger are all included in the total energy trigger events.   Let ε_1 be the efficiency of the total energy trigger for the multihadronic event.   Then, the probability that all the events of the coplaner track trigger are triggered by the total energy sum can be expressed by ε_1^{389}.   This probability should satisfy the following relation at the 95% confidence level.:

$$\varepsilon_1^{389} > 1 - 0.95 . \tag{5.9}$$

This relation requires the trigger efficiency of the total energy trigger to be:

$$\varepsilon_1 > (1 - 0.95)^{1/389} = 0.9933 . \tag{5.10}$$

On the other hand, out of 399 events of the total energy trigger, the coplanar track trigger missed 10 events.   Let ε_3 be the efficiency of the coplaner track trigger for the multihadronic events.   Then the probability that the coplaner track trigger misses less than 11 events out of 399 events is expressed as follows:

$$\sum_{N=0}^{10} \varepsilon_3^{399-N} (1 - \varepsilon_3)^N \, {}_{399}C_N . \tag{5.11}$$

where ${}_{399}C_N$ is the number of ditterent combinations possible of 399 items taken N at a time.

Then, at the 95% confidence level, the trigger efficiency of the coplaner track trigger is required to satisfy the relation,

$$\varepsilon_3 > 0.9575 . \tag{5.12}$$

This means that if ε_3 was less than this value, the probability in Eq. (5.11) should be less than 5% (*i.e.* we had observed a very rare phenomena).

The upper limit of the probability that both triggers miss a multihadronic event can be evaluated by taking into account the condition that these two triggers are independent.   The upper limit is $(1 - \varepsilon_1) \times (1 - \varepsilon_3) < 0.00033$, where the confidence level is more than 95%.   The probability must be smaller than this value because we have the segment energy sum trigger as the third multihadron event trigger.

In conclusion, the probability is so small that the trigger inefficiency can be ignored.

(D)   Event selection efficiency

The Monte Carlo simulations for the productions of the five known quarks and the t-quark were performed separately to estimate the efficiencies of the event selection. All these Monte Carlo data were processed by the same computer program as that for the real experimental data.

8000 Monte Calro events were generated for the production of the five known quarks with the LUND 5.3 model which includes the radiative corrections.   Among these simulated events, 6294 events remained after the preselection, and 5420 events
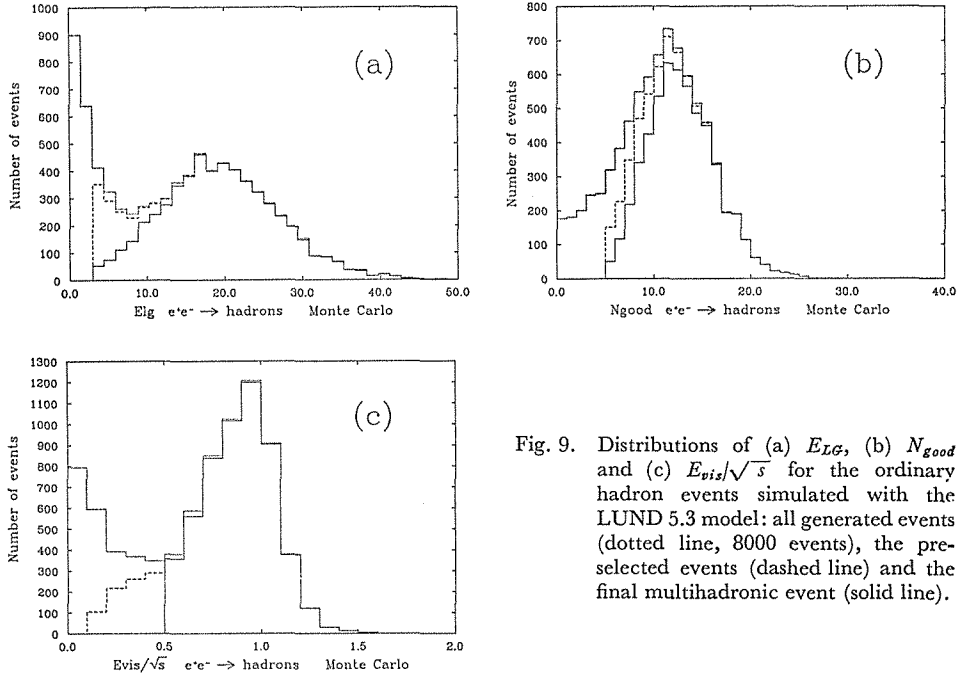
Fig. 9. Distributions of (a) E_{LG}, (b) N_{good} and (c) $E_{vis}/\sqrt{s}$ for the ordinary hadron events simulated with the LUND 5.3 model: all generated events (dotted line, 8000 events), the pre-selected events (dashed line) and the final multihadronic event (solid line).

finally remained after the multihadronic event selection. Fig. 9 shows the distributions of E_{LG}, N_{good} and $E_{vis}/\sqrt{s}$ for the Monte Carlo events. In this figure all the generated events, the preselected events and the finally selected events are shown by the dotted, dashed and solid histgrams, respectively. The selection efficiency was estimated to be 67.8% for the production of the five known quarks.

Since the predicted cross section of the production of the five known quarks is 187 pb from Eq. (4.5), the expected number of event remained after all the selections is calculated to be:

$$N_{exp} \text{ (5 flavour)} = \sigma \times \int L dt \times \text{efficiency} = 377 .\qquad (5.13)$$

The efficiencies for the open t-quark production were studied by assuming the t-quark mass (m_t) to be 23.0, 24.0, 25.0 and 25.5 GeV/c^2. 1000 Monte Carlo events were simulated at each mass. 994, 997, 993 and 995 events remained after the preselection for m_t=23.0, 24.0, 25.0, 25.5 GeV/c^2, respectively. 893, 898, 906 and 911 events remained after the multihadronic event selection. Then the efficiencies for the open t-quark production were found to be 89%, 90%, 91% and 91% depending on m_t. Thus the multihadronic event selection is proved to have a high efficiency for the open t-quark production, and the mass dependence is small in this mass region. The E_{LG}, N_{good} and $E_{vis}/\sqrt{s}$ distributions thus simulated are shown in Fig. 10 for m_t=25.5 GeV/c^2. The dotted, dashed and solid histograms indicate the distributions for all the generated events, the preselected events and the multihadronic events, respectively.
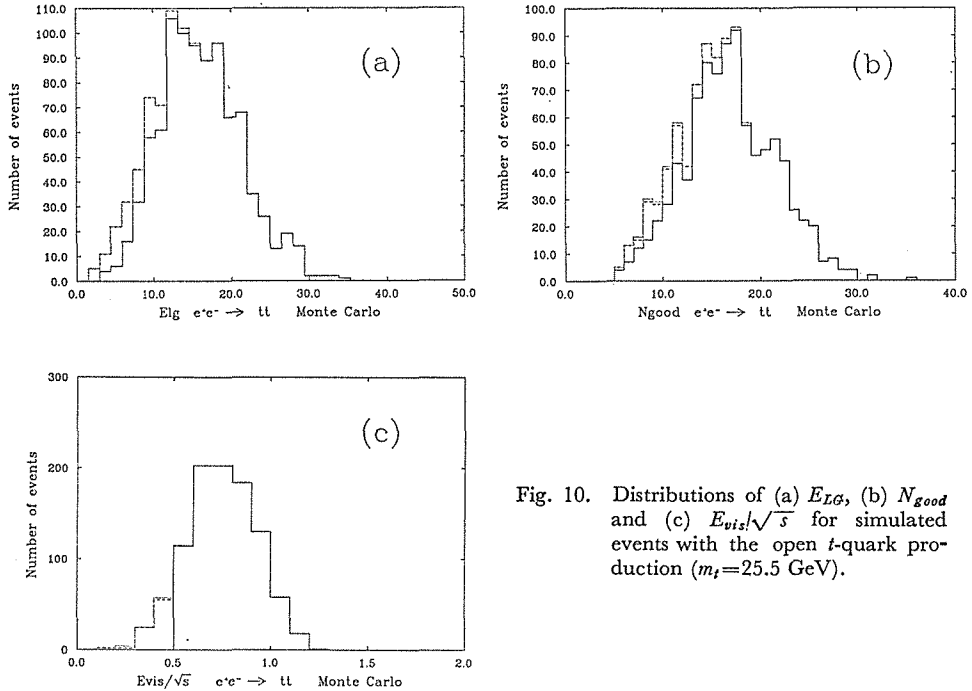
Fig. 10. Distributions of (a) E_{LG}, (b) N_{good} and (c) $E_{vis}/\sqrt{s}$ for simulated events with the open t-quark production ($m_t=25.5$ GeV).

As will be discussed in Section 5.4, the cross section of the open t-quark production is predicted to be 34 pb at $m_t=25.5$ GeV/c^2 considering the radiative correction factor of 0.8. The predicted number of the selected events for the open t-quark production is calculated to be

$$N_{expect}(top) = \sigma_{t\bar{t}} \times \int Ldt \times \text{efficiency} = 92 .\tag{5.14}$$

(E) Background

In order to estimate the background contamination in the observed multihadronic events, the Monte Carlo simulations for the two photon interaction ($e^+e^-\rightarrow e^+e^- +$ hadrons), and the τ pair production ($e^+e^-\rightarrow\tau^+\tau^-$) were carried out. In the two parton interaction, the generalized vector dominance model (GVDM) and the quark photon model (QPM) were used.

(F) Summary

Fig. 11 shows the $E_{vis}/\sqrt{s}$ distribution for the preselected events together with the results from the Monte Carlo simulation for the process of the multihadron production, two photon interaction and τ pair production, which are normalized by using the integrated luminosity and the cross sections. The number of the Monte Carlo events for the two photon interaction based on GVDM is normalized by fitting the lower region of the visible energy distribution ($E_{vis}<0.2\sqrt{s}$) to the observed data, because the cross section of this process has a large theoretical ambiguity.

The summary of the above Monte Carlo simulation is listed in Table-1, in which
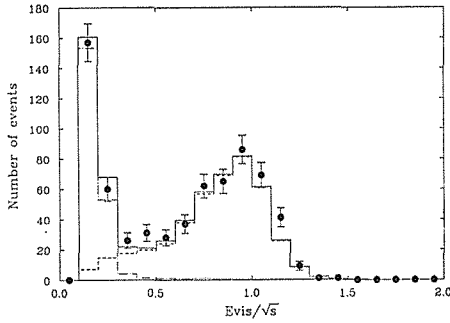
Fig. 11. Distribution of $E_{vis}/\sqrt{s}$ for the preselected events (closed circle) and the Monte Carlo events from the one photon exchange process (dotted histogram), the two photon interaction (dashed histogram) and the τ pair production (dashed-dotted histogram). The total contribution from the three processes is shown by a solid histogram.

Table 1. Summary of the Monte Carlo simulation for the hadronic event selection.

Processes	number of generated events	number of selected events	cross sections	number of expected events
five flavour	8000	5420	187 pb	377
open top-quark	1000	911	34 pb	92
two-photon GVDM	16000	0	300000 pb	small
two-photon QPM (u)	4000	12	160 pb	1.4
two-photon QPM (d)	500	2	10 pb	0.1
two-photon QPM (s)	500	3	10 pb	1.6
two-photon QPM (c)	3000	18	70 pb	1.3
two-photon QPM (b)	100	8	3 pb	small
tau pair	1000	32	45 pb	4.3

m_t is assumed to be 25.5 GeV/c^2.

The expected total number of events after all the selections is 386, assuming no t-quark production. Including the t-quark production with the cross section of 34 pb, the expected number of events amounts to 478. Therefore the observed number of 399 is consistent with the prediction from the five known quarks within the statistical error.

5.4. Shape analysis

(A) Shape parameters

In order to improve the sensitivity of the t-quark search, the shapes of the hadronic events were studied. In this study the backgrounds from the two photon processes and the τ pair productions were neglected because of their small contributions compared with the statistical error of the observed multihadronic events.

The quantities of Thrust(T), Acoplanarity(Ac) and Sphericity(S) were analysed in this study.

The definitions of T, Ac and other related parameters[5-3,4,5] are as follows:

$$T = \frac{\max_n \sum_j |\vec{p}_j \cdot \vec{n}|}{\sum_j |\vec{p}_j|} \,, \tag{5.15}$$

$$Ac = \frac{1}{4} \left[\frac{\min_e \sum_j |\vec{p}_j \cdot \vec{e}|}{\sum_j |\vec{p}_j|} \right]^2 \,, \tag{5.16}$$

$$M_j = \frac{\max_m \sum_j |\vec{p}_j \cdot \vec{m}|}{\sum_j |\vec{p}_j|} \,, \tag{5.17}$$

$$M_n = \frac{\sum_j |\vec{p}_j \cdot \vec{l}|}{\sum_j |\vec{p}_j|} \,, \tag{5.18}$$

where n is a unit vector which gives the maximum T and defines the thrust axis. m is a unit vector perpendicular to $\vec{n}$ giving the maximum M_j, and defines the major axis. $\vec{l}$ is a unit vector perpendicular to both $\vec{u}$ and $\vec{m}$, and defines the minor axis. $\vec{e}$ is also a unit vector which gives the minimum Ac, and defines the acoplanarity axis. $\vec{p}_j$ is a momentum vector of the j-th particle.

The definition of S is as follows:

$$S = \frac{3}{2} (Q1 + Q2) \,, \tag{5.19}$$

with

$$Qi = \frac{\lambda i}{\lambda 1 + \lambda 2 + \lambda 3} \qquad (i = 1, 2, 3) \,. \tag{5.20}$$

$\lambda 1$, $\lambda 2$ and $\lambda 3$ are the eigenvalues of the momentum tensor and the ordering is $\lambda 1 < \lambda 2 < \lambda 3$. The momentum tensor $M^{\alpha\beta}$ is a 3×3 matrix defined by the particle momentum as follows:

$$M^{\alpha\beta} = \sum_j p_j^\alpha p_j^\beta \qquad (\alpha, \beta = x, y, z) \,, \tag{5.21}$$

The momentum of the particles is weighted quadratically in the calculation of S, while it is weighted linearly in the calculations of T and Ac. The summation is taken over both charged and neutral particles which satisfy the following requirements.

For the charged particles, the condition of 'good tracks' (the criteria (a')–(d') in Section 5.3(A)) was required.

Fig. 12 shows the distribution of the momentum of track which satisfies the criteria (a'), (b') and (c') for the multihadronic events together with the Monte Carlo results normalized with the number of events. The Monte Carlo simulation well reproduces our observed distribution.

The neutral particles, which were assumed to be photons, were required to have the momenta larger than 0.2 GeV/c. The momenta of neutral particles were determined from the shower cluster energies in LG.

Fig. 13 shows the distribution of the cluster energy in the low energy region
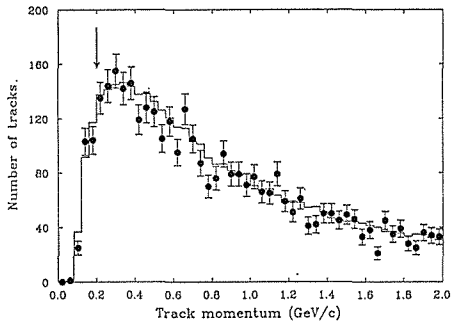
Fig. 12. Momentum distribution of the tracks
which satisfy the criteria described
in the text. The arrow indicates the
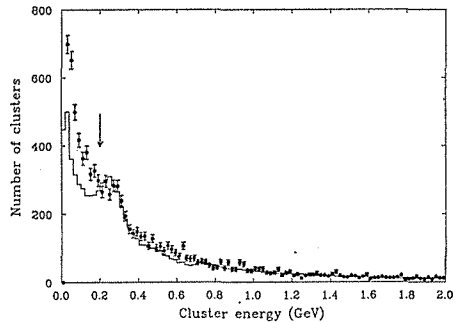cut line for the event shape analysis.

Fig. 13. Energy distribution of the energy of
the shower clusters. The arrow in-
dicates the cut line for the event
shape analysis.

together with the result of the Monte Carlo simulation normalized with the number
of observed events. The Monte Carlo simulation reproduces well our observed
distribution in the selected region of larger than 0.2 GeV.

T represents the degree of collimation of the final particles in two jets, while Ac
represents the degree of deviation from a planer shape. S represents deviation from
the shape of narrow two jets. The thrust axis $(\vec{n})$ represents the direction of the two
jets in which the momentum flow is collimated back-to-back. The 'event plane' is
defined by the thrust and major axes, and it is perpendicular to the minor axis. In
an event which has a planer shape such as a three-jet event, the momentum flow
distributes in this plane.

The masses of the five known quarks are much less than the present beam energy.
Therefore, the $q\bar{q}$ events have large T, small Ac and small S. The shape of three-jet
events from the $e^+e^- \rightarrow q\bar{q}g$ process, in which a hard gluon is emitted with a large
angle with respect to the directions of the quarks, are expected to be flat. Such
events have small T, small Ac and large S.

On the other hand, the events with the open t-quark productions tend to have
small T, large Ac and large S, because the decay products from the t-quarks are
emitted with large angles each other near the threshold energy region. This means
that both the events with t-quark production and the three jet events have small T and
large S. Therefore, Ac is expected to be sensitive for the t-quark search. It should
be noticed that the four jet events are expected to have a large Ac, however the cross
section of four jet events is very small compared with the three jet events.

(B) Event selection for the shape analysis

For the event shape study, the following two more cuts are applied to the multi-
hadronic events selected previously.

(1) $|\cos \theta_T| < 0.7$, where θ_T is the polar angle of the thrust axis.

(2) $|\cos \theta_n| > 0.15$, where θ_n is the polar angle of the minor axis.

The cut (1) selects the events in which most of the final particles are within the
detector acceptance for the two-jet events. The ratio of the energy flow into the
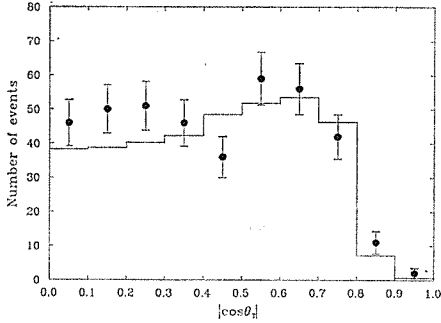
Fig. 14. Distribution of $|\cos\theta_T|$ for the observed events (closed circle), and the simulated events (histogram).
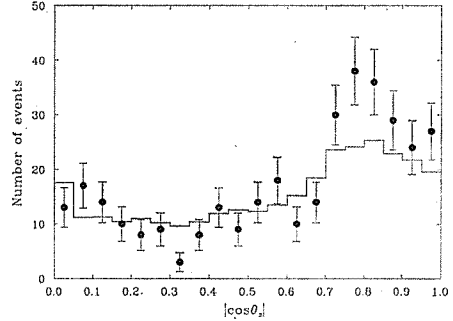
Fig. 15. Distribution of $|\cos\theta_n|$ for the observed events (closed circle), and the simulated events (histogram).

acceptance of the barrel calorimeter to the total energy was calculated by the Monte Carlo simulation with the LUND 5.3 model for the production of the five known quarks. The result shows that most of the energy flow is detected by LG for the events with $|\cos\theta_T| < 0.7$.

The observed distribution of $|\cos\theta_T|$ is shown in Fig. 14, together with the prediction by the Monte Carlo simulation with the five known quarks (LUND 5.3).

The cut (2) aims to reject the event with an initial hard radiation emitted into the direction of the beam axis. The event planes for the events with such initial hard radiations include the beam axis, so that the minor axis is perpendicular to the beam axis by the definition.

The $|\cos\theta_n|$ distributions were calculated by the Monte Carlo simulation. It was found that the cut value of 0.15 is reasonable to reject events with the initial hard radiation. The observed $|\cos\theta_n|$ distribution is shown in Fig. 15, together with the result of the Monte Carlo simulation.

Out of 399 multihadronic events, 300 events remained after these selections.

(C) Distributions of event shape parameters

The T, Ac and S distributions for the multihadron events after the cuts are shown in Fig. 16 together with the results of the Monte Carlo simulation with the five known quark model (solid histogram) and with the six quark model including the open t-quark pair production (dashed histogram). The Monte Carlo events are normalized to the integrated luminosity of 2.9 pb^{-1}. The t-quark mass was assumed to be 25.5 GeV/c^2 and the cross section of the open t-quark production was assumed to be 34 pb which will be discussed later. As a whole, the five known quark model is consistent with the present data.

However, the Ac distribution obtained from the Monte Carlo simulation by the LUND 5.3 model with the five known quarks agrees poorly with the observed distribution. The observed distribution has larger values of Ac than the prediction by the Monte Carlo simulation.

The dependence of the Ac distribution on the parton production and fragmentation schemes in the Monte Carlo simulation was studied for three different models.
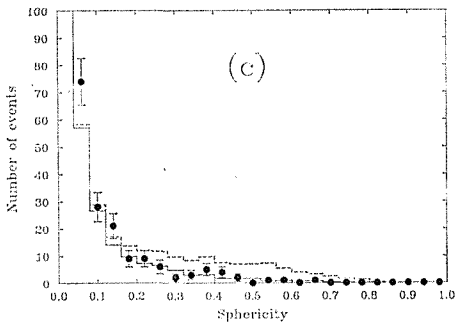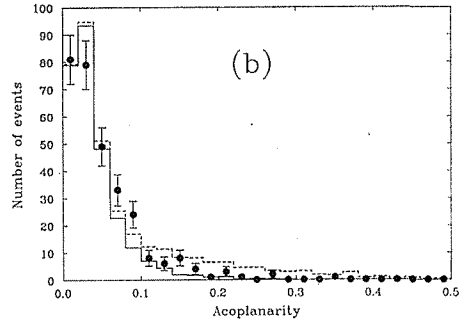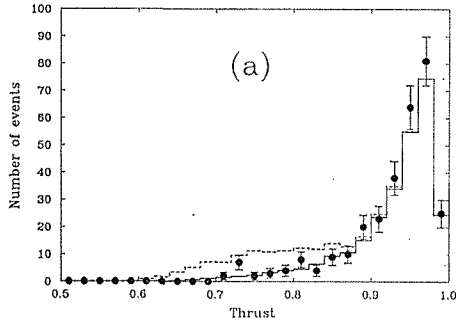
Fig. 16. Distributions of (a) Thrust, (b) Aco-
planarity and (c) Sphericity. The
observed data (closed circle) are
compared with the results of the
Monte Carlo simulation of the five
known quark production (solid hist-
ogram) and the six-flavour (five
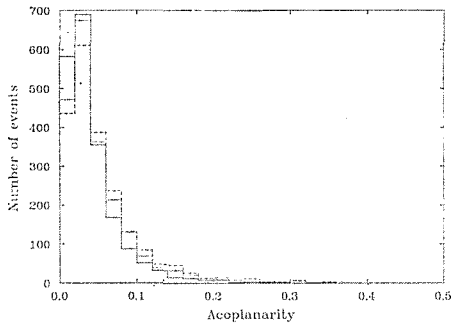known quarks and t-quark) produc-
tion (dashed histogram).

Fig. 17. Acoplanarity distribution for the
Monte Carlo evens from the five
known quark production for the
three different models, which are the
LUND 5.3 model (solid histogram),
the LUND 6.3 model (dashed histo-
gram) and the WEBBER model
(dotted histogram).

(a)   (b)
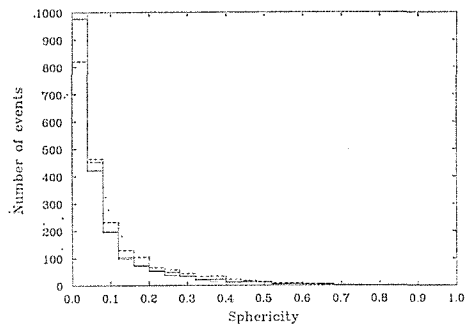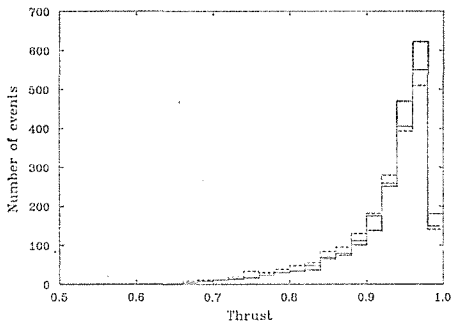
Fig. 18. Distributions of (a) Thrust and (b) Sphericity for the Monte Carlo evens from the five
known quarks production for the three different models, which are the LUND 5.3 model
(solid histogram), the LUND 6.3 model (dashed histogram) and the WEBBER model
(dotted histogram).

The results are shown in Fig. 17.   The solid, dashed and dotted histograms are the results from the LUND 5.3, LUND 6.3 and WEBBER models, respectively.   They indicate that the LUND 5.3 model gives the thinner event shape than the other two models.   The LUND 6.3 and WEBBER models show a good agreement with the present results.

The T and S distributions do not depend so much on the parton production and fragmentation schemes.   These distributions predicted by the LUND 5.3, LUND 6.3, and WEBBER models are shown in Fig. 18.   The results of these three models agree with the present results within the statistical error.

As will be shown later, the Ac distribution for the open t-quark production has a small model-dependence.   Due to the heavy mass of the t-quark, the event shape is determined mainly by the decay kinematics of the t-quark rather than the parton production and fragmentation schemes.

(D)   Efficiency for the Acoplanarity cut

As was stated in Section 5.4 (A), the Ac distribution was studied to search for the signature of the open t-quark production.   The event with the t-quark production is calculated with the Monte Carlo simulation.   These events are expected to have large values of Ac.   The cuts applied to the observed events were also applied in this simulation.   The detection efficiency of the events with t-quark production was evaluated by the simulation and it is found that the efficiency depends on the mass of the t-quark.   Near the threshold energy, the efficiency becomes smaller for the heavier mass of the t-quark.

Fig. 19 shows the Ac distributions for the events with the open t-quark production calculated by the LUND 5.3 model for different values of t-quark mass m_t.   The solid, dashed and dotted histograms correspond to m_t=25.5, 25.0 and 24.0 GeV/c^2, respectively.   The mass dependence of the efficiency are shown in Fig. 20 for the

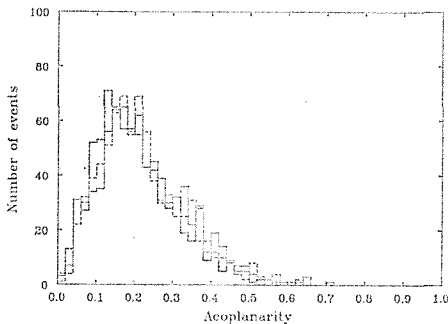

Fig. 19.   Acoplanarity   distribution   for   the Monte Carlo events from the open t-quark production; $m_t = 25.5$ GeV (solid   histogram), $m_t = 25$ GeV (dashed histogram) and m_t=24 GeV (dotted histogram).
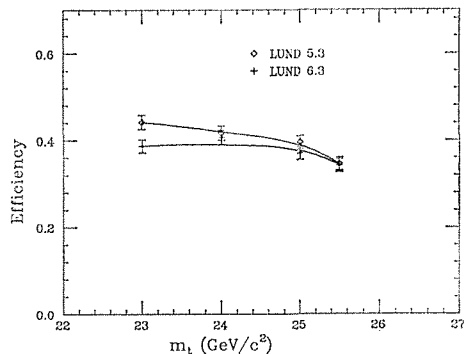
Fig. 20.   Efficiencies for the $Ac > 0.2$ cut calcu lated by the Monte Carlo simulation with the open t-quark production. The efficiencies are plotted as a function of the t-quark mass, m_t, for the two models (LUND 5.3 and LUND 6.3).
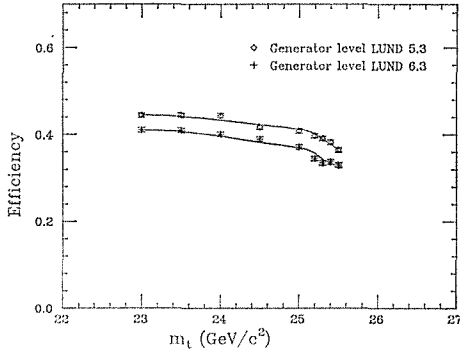
Fig. 21. Efficiencies for the $Ac>0.2$ cut calculated by the generator level simulation with the open t-quark production. The efficiencies are plotted as a function of the t-quark mass, m_t, for the two models.
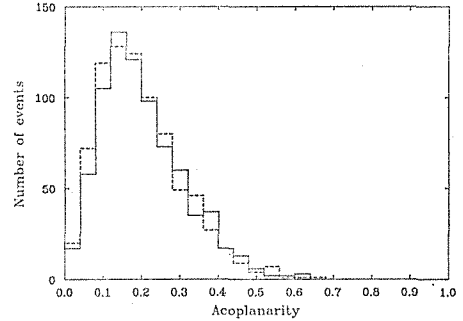

Fig. 22. Acoplanarity distribution for the Monte Carlo events from the open t-quark production at $m_t=25.5$ GeV. The results of the LUND 5.3 and LUND 6.3 models are also shown by the solid and dashed histgrams, respectively.

events with $Ac>0.2$ near the threshold energy.

The so called 'generator level' simulation was used to study the parameter dependence in the open t-quark production instead of the VMONT. In this calculation the measured energy, momentum and direction of particles are calculated directly from the event generated by the event generator. The effects of the acceptance and the resolution of each detector were folded into this calculation. This method is not fully realistic like the VMONT, but it was found to be useful for saving the computer CPU time without losing the accuracy. The mass dependences calculated by this method are shown in Fig. 21, and they agree well with those by VMONT in Fig. 20.

If a pair of topped mesons ($t\bar{u}$ or $t\bar{d}$ mesons) are produced at the threshold energy of $\sqrt{s}=52$ GeV, then the mass of the topped meson is 26 GeV/c^2. Taking into account the mass of u or d-quark (0.3 GeV/c^2), the mass of the the t quark in the topped meson is 25.7 GeV/c^2 in this case.

The efficiency for the events with $Ac>0.2$ at the threshold energy was obtained to be 0.33 by extrapolating the curve in Fig. 20 to $m_t=25.7$ GeV/c^2.

(E) Systematic error of the detection efficiency
(1) Model dependence

The model dependence of the efficiency is regarded as one of the sources of the systematic error. The LUND 6.3 model with the open t-quark production was compared with the LUND 5.3 model. The Ac distribution from the LUND 6.3 with $m_t=25.5$ GeV/c^2 is shown in Fig. 22 (the dashed histogram) together with that from the LUND 5.3 model (the solid histogram). The mass dependence of the efficiency for the cut of $Ac>0.2$ from the LUND 6.3 model is shown in Fig. 20. The mass dependence from the 'generator level' simulation by the LUND 6.3 model is also shown in Fig. 21. The difference between the two models at $m_t=25.7$ GeV/c^2 is 5% of the above estimated efficiency (0.33).

(2)   Fragmentation parameter dependence

The parameter dependence of the efficiency was also investigated by changing the values of parameters a, b, σ_{pt}, Y_{min} and Λ_{QCD} within the reasonable regions.   The results from the LUND 5.3 and LUND 6.3 models are shown in Fig. 23 and Fig. 24,
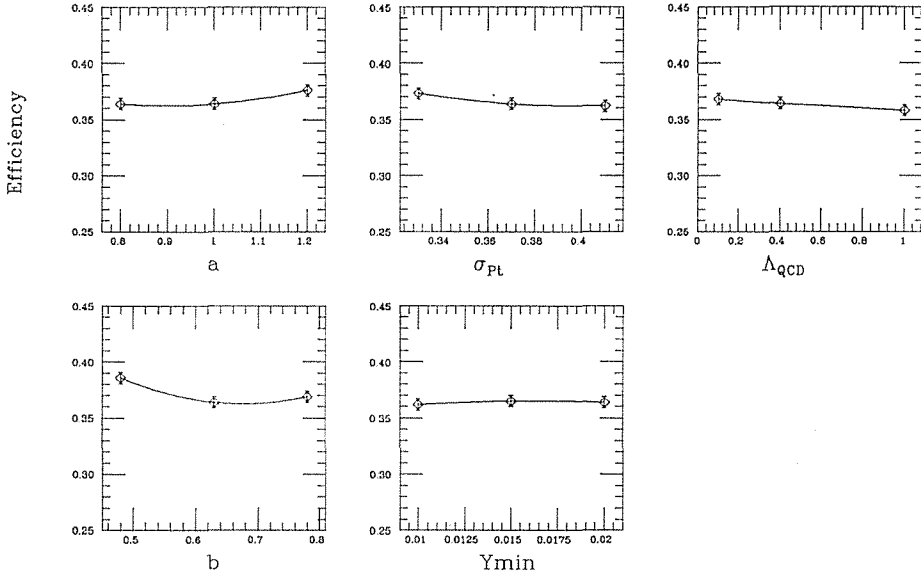

Fig. 23.   Parameter dependence of the efficiency for the $Ac < 0.2$ cut calculated by the generator level simulation with the open t-quark production by using the LUND 5.3 model.
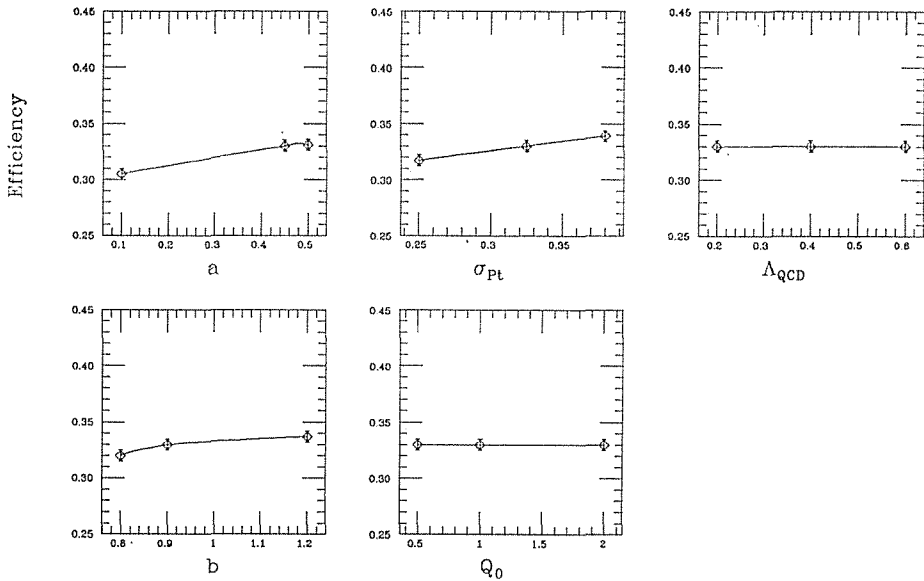

Fig. 24.   Parameter dependence of the efficiency for the $Ac > 0.2$ cut calculated by the generator level simulation with the open t-quark production by using the LUND 6.3 model.

respectively.   The parameter dependence was found to be at most 9% (LUND 5.3) and 10% (LUND 6.3) by combining the contributions of all the parameters in quadrature.   Thus, the systematic error due to the ambiguities of the parameters was finally determined to be 10%.

(3)   Cut dependence

The uncertainties of the quantities as E_{LG}, N_{good}, E_{vis}, $|\cos\theta_T|$, $|\cos\theta_n|$ and Ac used for the event selections were estimated taking into account the resolution of detectors.   For each event in the Monte Carlo simulation with the open t-quark production, momenta, energies and directions of all tracks and all shower clusters were independently changed assuming the detector resolutions of the gaussian type. The distributions of the deviations from the initial values were calculated for each quantity.   Two times of the root mean square of the distribution was regarded as the uncertainty.   The uncertainty of N_{good} was assumed to be at most 1.   The uncertainties thus estimated are summarized as follows:

$$\Delta E_{LG} = 0.7 \text{ GeV},$$

$$\Delta N_{good} = 1,$$

$$\Delta E_{vis} = 0.02 \times \sqrt{s},$$

$$\Delta |\cos\theta_T| = 0.017,$$

$$\Delta |\cos\theta_m| = 0.009,$$

$$\Delta Ac = 0.012.$$

The cut dependence of the efficiency is shown in Fig. 25 for each quantities.

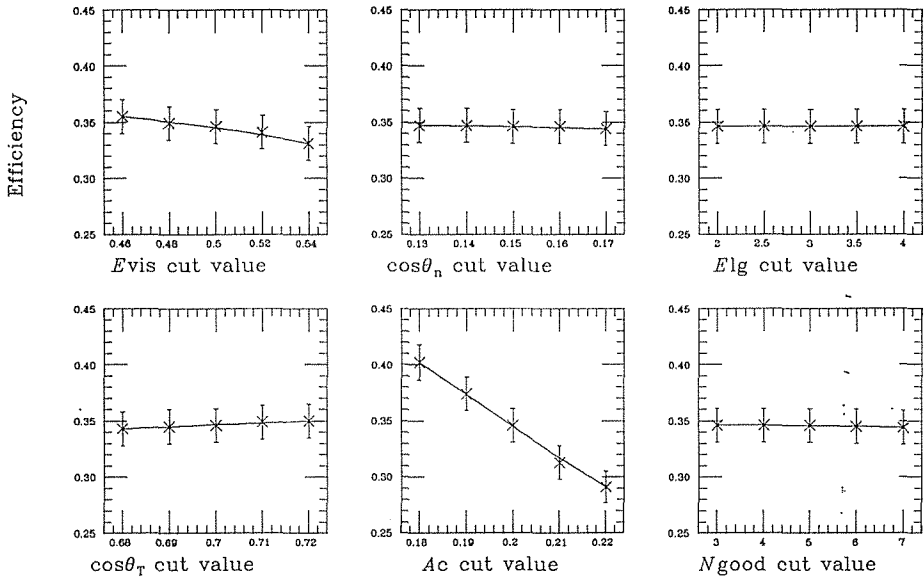Fig. 25.   Cut value dependence of the efficiency for the open t-quark production events around the used cut values.

The error of the efficiency due to the above uncertainties for each cut value was found to be as follows:

$$E_{LG} \rightarrow \text{negligibly small,}$$
$$N_{good} \rightarrow \text{negligibly small,}$$
$$E_{vis} \rightarrow 1.5\%,$$
$$|\cos \theta_T| \rightarrow 1\%,$$
$$|\cos \theta_n| \rightarrow \text{negligibly small,}$$
$$Ac \rightarrow 13\%.$$

The largest error comes from the uncertainty of the Ac cut (13%). The total error of the efficiency due to the uncertainties of the cuts is evaluated to be 16% by taking a linear summation.

(4) Uncertainty of t-quark decay

The present Monte Carlo simulations assume that the t-quark decays only into a b-quark and a virtual W-boson as $t \rightarrow b + W^*$. However the efficiency for the events with $Ac > 0.2$ decreases if the t-quark can decay into a d-quark or an s-quark such as $t \rightarrow d + W^*$ or $t \rightarrow s + W^*$, because the mass of the d-quark or the s-quark is very light compared with the b-quark mass and then the Ac distribution tends to be narrower than the case of $t \rightarrow b + W^*$ decay. The decay branching ratio of the t-quark can be estimated from the Kobayashi-Maskawa matrix elements, which mean the magnitudes of the couplings between the different quarks. The couplings of the b-quark to the u- and c-quarks have been found to be less than 0.054 from the measurements of the life time of the b-mesons[5-6]. Therefore, the coupling between the b-quark and the t-quark is larger than $\sqrt{1-0.054^2}$, assuming only three generations. Then the decay branching ratio of $t \rightarrow d$ or $t \rightarrow s$ is estimated to be less than 0.0029 ($=0.054^2$). In conclusion, the contribution of the decay modes of the t-quark into the light quarks (d or s) is negligibly small.

(5) Statistical error of the Monte Carlo simulation

The statistical error of the Monte Carlo simulation was estimated to be 3% (two times of the root-mean-square), and this must be included in the systematic error of the efficiency.

(6) Summary

By combining all these ambiguities in quadrature, the total systematic error amounted to be 20% as is summarized in Table 2.

Finally, the efficiency is represented as follows:

$$\varepsilon(Ac > 0.2) = 0.33 \times (1 \pm 0.20) . \tag{5.22}$$

(F) Search for the t-quark production

The expected number of event after the cut of $Ac > 0.2$ can be expressed as follows:

$$N_{expect} = \sigma_{t\bar{t}} \times (1+\delta) \times \int L dt \times \varepsilon , \tag{5.23}$$

Table 2.   Summary on the systematic error of the efficiency for
the Acoplanarity cut.

Source of errors	%
Model dependence	5
Fragmentation parameters	10
Cut values	16
Decay branching ratio	small
Statistical error of the M.C.	3
Total	20

where $\sigma_{t\bar{t}}$ is the cross section of the open t-quark production. $(1+\delta)$ is the factor of the radiative correction. ε is the efficiency for the cut of $Ac > 0.2$. The quantity of $\int Ldt$ expresses the integrated luminosity. Substituting Eq. (5.7) and (5.22), Eq. (5.23) becomes as follows:

$$N_{expect} = \sigma_{t\bar{t}} \times (1+\delta) \times 2.90 \times 0.33 \times (1 \pm 0.21), \qquad (5.24)$$

where the error includes the errors of the integrated luminosity which has the systematic error of 6% and the statistical error of 3%.

The expected cross section of the t-quark pair production near the threshold energy is calculated by the expression given in Appendix I. Neglecting the QCD effect, the cross section, which is given by Eq. (A.1), (A.2) and (A.3), becomes zero at the limit of $m_t \rightarrow E_{beam}$.

The first order QCD effect gives a term of β^{-1} to the cross section as is shown in Eq. (A.6) and (A.7). Then, the cross section at the limit of $m_t \rightarrow E_{beam}$ can be expressed as follows:

$$\sigma_{t\bar{t}}(QCD) = \pi^2 \{ (4\pi\alpha^2/s)Q_q^2 + (4G_F\alpha/\sqrt{2})Q_t g_v^e g_v^t Re(\chi)$$
$$+ (G_F^2/2\pi)(g_v^{e2} g_a^{e2})g_v^{t2} s|\chi|^2 \}, \qquad (5.25)$$

where the meaning of parameters are given in Appendix I. Actually, the cross section has the resonance effect near the threshold energy. The calculation of the cross section including the resonance effect depends strongly on the resonance models. Suppose that the cross section rises as a step function at the threshold energy averaging the couplings with resonances, then $\sigma_{t\bar{t}}$ is calculated to be 43 pb, which comes mainly from the vector coupling part (σ_{VV}) in Eq. (A.6) at the $m_t \rightarrow E_{beam}$ limit. The axial vector part (σ_{AA}) is negligibly small because this part has the β^3 dependence as is shown in Eq. (A.3). The S-wave quark-antiquark state can not be the axial vector state, so that the coupling with axial vector resonances is very small near the threshold energy[5-7].

The QED radiative correction factor $1+\delta$ was calculated according to the method by Behrends, Kleiss and Jadach[3-5] up to the first order. This factor de-

creases steeply near the end point of m_t, and finally becomes less than zero, whose value has no physical sense. This means that the approximation up to the first order correction is unreasonable at just above the threshold energy. Then the value of $1+\delta$ was chosen at the quark mass of 25.5 GeV/c^2. The estimated value is 0.8 at the beam energy of 26 GeV.

From the values of $\sigma_{t\bar{t}}=43$ pb and $(1+\delta)=0.8$, the expected number of events with $Ac>0.2$ was obtained by using Eq. (5.24) for the t-quark mass of 25.5 GeV/c^2 as:

$$N_{expect} = 33\pm7 . \tag{5.26}$$

By comparing this expected number of events (33 ± 7) with the observed number of events (7), it is concluded that the open t-quark production can be excluded at the present energy of $\sqrt{s}=52$ GeV.

The expected number of events with $Ac>0.2$ from the five known quark productions is calculated to be 2.4 by the LUND 5.3 model. This value is small compared with the observed number of 7. In the five known quark production, the four-jet event associated with QCD such as $e^+e^-\rightarrow q\bar{q}gg$ and $e^+e^-\rightarrow q\bar{q}q\bar{q}$ gives the large Ac. Feynman diagrams of these processes are shown in Fig. 3. It was reported[5-8,9] that the cross sections of these processes were underestimated in the LUND 5.3 model. One of the motivations to upgrade the LUND model from the matrix element method (LUND 5.3) to the parton shower method (LUND 6.3) came from this problem. In fact, the expected number of events with $Ac>0.2$ are calculated to be 7.2 and 4.2 from the LUND 6.3 and WEBBER models, respectively.

Then the observed number of events with $Ac>0.2$ is consistent with the five flavour hypothesis.

(G)   Upper limit of $\sigma_{t\bar{t}}$

The upper limit of the cross section including the radiative corrections, (*i.e.* the measured cross section) is estimated in the following. The $Ac>0.2$ cut is also used here.

The Ac distribution predicted by the Monte Carlo simulation with the five known quarks depends strongly on the parton production and fragmentation scheme as mentioned above, and the statistics is poor in the region of $Ac>0.2$. Therefore, the number of events in the region of $Ac>0.2$ can not be estimated accurately in this case.

In this experiment, 7 events were observed in the $Ac>0.2$ region. In consequence, the number of events, which is expected by the 'true' theory, should be less than 13.2 at the 95% confidence level. This limit is obtained by assuming the Poisson statistics.

From Eq. (5.24), the upper limit at the 95% C.L. can be calculated as follows:

$$\sigma_{t\bar{t}}\times(1+\delta)<\frac{13.2}{2.90\times0.33\times(1-0.21)} = 17 \text{ pb} . \tag{5.27}$$

In the estimation of the upper limit, all the observed events with $Ac>0.2$ were assumed to come from the open t-quark production. The possible contaminations

from the ordinary processes were not taken into account.   If the contaminations were reduced from the observed events, the smaller upper limit would be obtained.

6.   Discussion and conclusion

The multihadronic production in the electron-positron interaction, $e^+e^- \rightarrow$ hadrons, have been measured at the center-of-mass energy of 52 GeV.   The shape of these multihadronic events was analyzed to search for the signature of open t-quark production.

If the t-quark production channel opens at this energy, the multihadronic events with low thrust, high sphericity and high acoplanarity are expected to be observed at higher rate, because t-quarks will be produced almost at rest and the decay products from them tend to distribute spherically.

The similar analyses were performed in the energies from 10 GeV to 43 GeV at PEP and PETRA.   The average values of thrust and sphericity measured at PETRA are shown in Fig. 26[1-4].   As the beam energy increases, the average value of thrust increases, while that of sphericity decreases.   This can be naturally understood by the interpretation that decay products from a b- or c-qurak are boosted more strongly to the direction of the parent quark as the center-of-mass energy increases.

The present average values of thrust and sphericity obtained by this experiment are also plotted in these figures together with the predictions from the Monte Carlo simulation with or without the t-quark production.   Our results fall on the extention from the low energy results.   It should be noted that these values can not be directly compared with the data of PETRA, because the average value of thrust and sphericity depend on the acceptance of the detector and the event selections.

From the shape distributions as shown in Fig. 16, no enhancement of events with low thrust, high sphericity and high acoplanarity was observed.   Then, it can be concluded that there is no evidence for the t-quark production and these distributions are consistent with the five known quark hypothesis.

The quantitative analysis was performed with the acoplanarity distribution, and
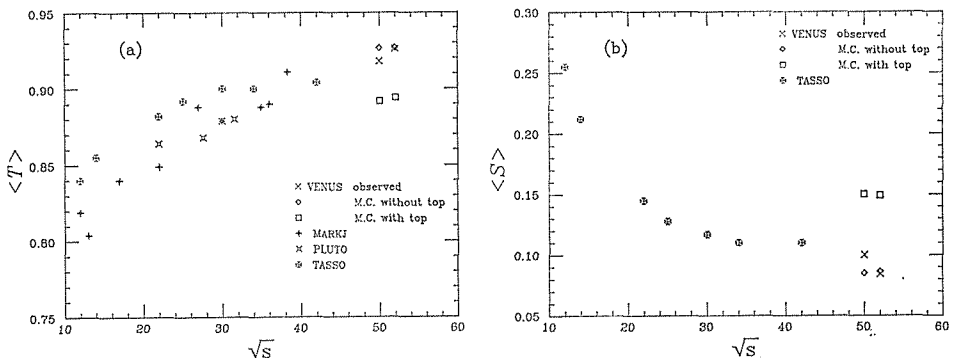

Fig. 26.   Average values of (a) Thrust and (b) Sphericity in PETRA and TRISTAN energies.   The differences due to the detector acceptances are not corrected.

the open t-quark production with the expected cross section of 34 pb, assuming $m_t = 25.5$ GeV/c^2, is rejected. The upper limit of the cross section of the open t-quark production is 17 pb at the 95% confidence level.

Acknowledgment

Appendix

I. Cross section of hadron production

The cross section of the quark anti-quark pair production $(e^+e^- \rightarrow q\bar{q})$ is calculated as follows, ignoring the QCD effects and the resonance effects[(4-1)].

$$\sigma_{q\bar{q}}(QED) = \sigma_{VV} + \sigma_{AA}, \tag{A.1}$$

where σ_{VV} and σ_{AA} represent the vector coupling part and the axial vector coupling part, respectively. σ_{VV} and σ_{AA} can be expressed explicitly as,

$$\sigma_{VV} = (1/2)(3\beta - \beta^3)\{(4\pi\alpha^2/s)Q_q^2$$
$$+ (4G_F\alpha/\sqrt{2})Q_q g_v^e g_v^q Re(\chi)$$
$$+ (G_F^2/2\pi)(g_v^{e2} g_a^{e2})g_v^{q2}s|\chi|^2\}, \tag{A.2}$$
$$\sigma_{AA} = \beta^3(G_F^2/2\pi)(g_v^{e2} g_a^{e2})g_a^{q2}s|\chi|^2, \tag{A.3}$$

where β is the velocity of the quark and calculated as $\beta = \sqrt{1 - m_q^2/E_{beam}^2}$. G_F is the Fermi coupling constant, and χ is expressed as

$$\chi = M_Z/(M_Z^2 - s + iM_Z\Gamma_Z), \tag{A.4}$$

where M_Z and Γ_Z denote the mass and the width of Z-boson and s is the squared center-of-mass energy. Coupling constants are given from the standard model of the electro-weak interaction as

$$g_v^{e,q} = \mp 1/2 - 2Q_{e,q}\sin\theta_W^2 , \quad g_a^{e,q} = \mp 1/2 , \tag{A.5}$$

where the minus signs are for the electron and the quarks with negative charge, while the plus signs are for the quarks with positive charge. Q_e and Q_q represent the charge of the electron and the charge of the quark, respectively.

Including the QCD effect up to the second order processes such as $e^+e^- \to q\bar{q}$, $q\bar{q}g$, $q\bar{q}q\bar{q}$ and $q\bar{q}gg$, the total cross section is written as

$$\begin{aligned}
\sigma(QCD) &= (1 + C_1^V\alpha_S/\pi + C_2^V(\alpha_S/\pi)^2)\sigma_{VV} \\
&\quad + (1 + C_1^A\alpha_S/\pi + C_2^A(\alpha_S/\pi)^2)\sigma_{AA} ,
\end{aligned} \tag{A.6}$$

where the values of the first order correction factor $(C_1^V$ and $C_1^A)$ and the second order correction factor $(C_1^V$ and $C_1^A)$ are as follows:

$$\begin{aligned}
C_1^V &= (4/3)\pi\{\pi/2\beta - ((3+\beta)/4)(\pi/2 - 3/4\pi)\} , \\
C_1^A &= 1 , \quad C_2^V = C_2^A = 1.39 .
\end{aligned} \tag{A.7}$$

In this study, the following values are used to calculate the cross sections.

$$M_Z = 92.5\,\text{GeV} , \tag{A.8}$$

$$\Gamma_Z = 2.7\,\text{GeV} , \tag{A.9}$$

$$\sin\theta_W^2 = 0.226 , \tag{A.10}$$

$$\alpha_S(\sqrt{s} = 50\,\text{GeV}) = 0.17 \quad (\overline{MS}\text{ scheme}) . \tag{A.11}$$

II. Inner chamber (IC)

The inner chamber is the innermost detector of VENUS, and it is designed not only to measure the trajectories of emerging particles from the interaction point but also to provide a fast and efficient 'z-trigger' signal for selecting the events which originate from the interaction point and for rejecting backgrounds such as cosmic rays, beam-gas events and beam-beampipe events.

The inner chamber is a cylindrical drift chamber of six layers. The structure of the chamber is shown in Fig. A-1. The dimension is listed in Table A-1. There are 640 anode wires of 30 μm in diameter made of gold plated tungsten and 640 field wires of 120 μm in diameter made of copper beryllium. The half gap of the chamber is 5 mm, and the wire spacing is about 5 mm. The cell geometry is shown in Fig. A-2.

Special cares were paid to reduce a total amount of materials in order to minimize interactions of particles in the chamber. Seven cathode cylinders, each of which is 1628 mm in length and 6 mm or 18 mm in thickness, were coaxially fixed to 12 mm thick aluminum end-plates. The cathode cylinder has a 'honeycomb' structure made of paper with cathode sheets glued on both surfaces. The cathode sheets were

fabricated from 125 μm thick Kapton sheets laminated by 18 μm thick copper on both sides. A pattern of cathode pad is etched on the surface, and readout-lines are etched on the back surface. The outer surfaces of the innermost and outermost
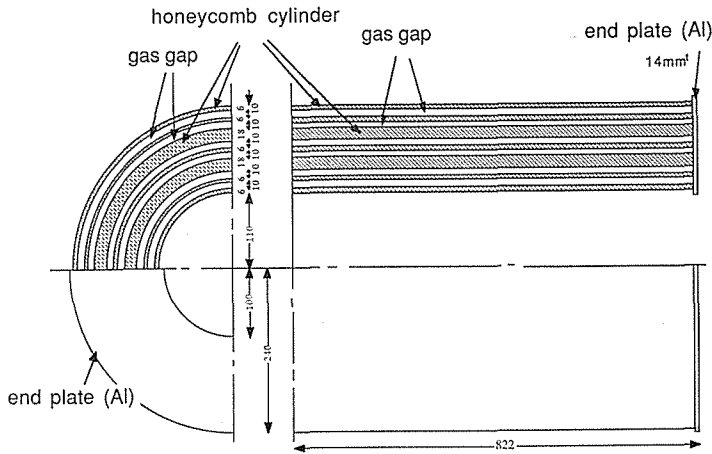

Fig. A–1. Structure of the inner chamber.

Table A–1. Dimension of the Inner Chamber

(a) General

number of layers	6
number of of honeycomb cylinders	7
total number of anode wires	640
total number of field wires	640
total number of cathode pads	768
segmentation of cathode of each layer	8 (φ)–16 (z)
length of sensitive region	160 cm
radius of inner wall	11.0 cm
radius of outer wall	23.6 cm
diameter of anode wire	30 μm
diameter of field wire	120 μm

(b) Dimension of each layer

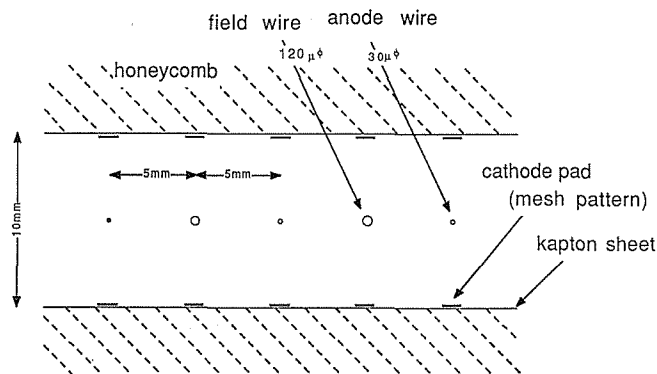| layer	radius of wire planes	number of anode wires	length of each cathode pads (z-direction)
1	121 mm	80	52.2 mm
2	137 mm	80	59.2 mm
3	165 mm	96	71.2 mm
4	181 mm	112	78.0 mm
5	209 mm	128	90.1 mm
6	225 mm	144	97.0 mm

Fig. A-2.   Cell geometry of the inner chamber.

cylinders are 50 μm Kapton laminated by 18 μm copper on only the one side.   The total amount of material perpendicular to the beam axis is less than 0.03 radiation lengths.

The gas of $Ar/CO_2/CH_4$ (49%/50%/1%) is filled in the chamber at the atmospheric pressure.   The gas is chosen by taking account of the result of the aging test[2-3] performed with the test chambers.   In this test, the test chambers were radiated by a collimated high intensity beta-ray beam from a 1 mCi Sr^{90} source.   Several kinds of gas mixture were tested.   For the gas mixture which contains much hydrocarbon, such as Ar/C_2H_6 (50%/50%), discharges between wires were observed frequently after the irradiation.   Once the discharge starts, the wire chamber could no longer be operated at high voltage.   Therefore, CO_2 gas was chosen as a quencher instead of hydrocarbon gas.

The configuration of cathode pads is shown in Fig. A-3.   To provide a z-trigger, signals of cathode pads of each layer are read out.   The cathode plane of the outermost layer (the sixth layer) is divided eventually into 16 elements in the z-direction and into 8 elements in the φ-direction.   Then the cathodes of other inner layers are
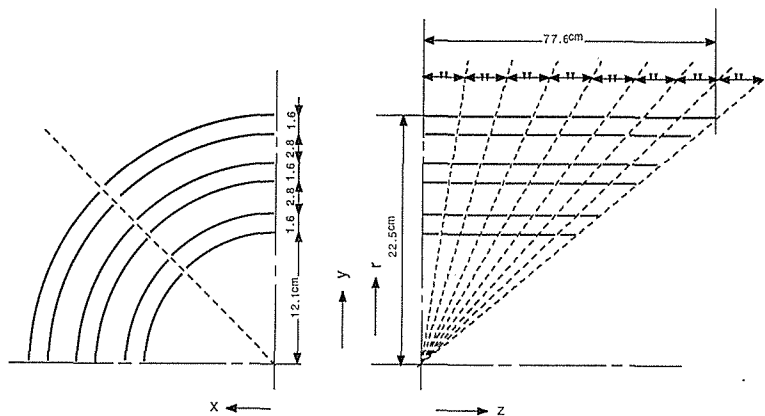

Fig. A-3.   Cathode pad configuration of the inner chamber.

divided such that they cover the same solid angles as those of the pads of the 6th layer. There are 768 pads (6-layer × 16-z × 8-φ) in total. A set of six pads in the same solid angle viewing from the interaction point is called 'tower'. A charged particle emitting from the interaction point hits six pads in a tower. However, the charged particle which is not produced at the interaction point hits six pads belonging to different towers. As a result, the hit pattern of the towers provides the information whether there are charged particles going out from the interaction point or not.

The performances of triggering for the above inner chamber were studied by a Monte Carlo simulation. Fig. A-4 shows the detection efficiency as a function of the z-coordinate for the events which are produced by the beam-beampipe inter-action and have a hit at least one 'tower'. The events produced at the position far from $z=0$ are rejected as is shown in the figure. Therefore, the requirement of the hit of at least one 'tower' is included in the z-trigger.

The signal from each pad is transmitted to a preamplifier placed directly on the end-plates of the chamber, and then transmitted to an amplifier-discriminator module through 47 m long shielded twisted-apir cable. The output signals from all dis-criminators (768 channels) are sent to a trigger processor. The trigger processor provides a trigger signal if the hit pattern of the pads matches with the data written in the 'look at table' of RAM's. The decision time of the trigger is less than 2.5 μsec after the beam crossing. The output signals from all discriminators are also sent to FASTBUS modules named Memory Partner, and then recorded into the VAX-11/780 computer.

Signals from anode wires are amplified by preamplifiers placed on the end plates of the chamber, and transmitted to amplifier-discriminator modules through the same type of calbles as those for cathode signals. The output signals from all dis-criminators are sent to a TAC-ADC system in FASTBUS, then the hit pattern and the digitized timing information are sent to VAX-11/780.
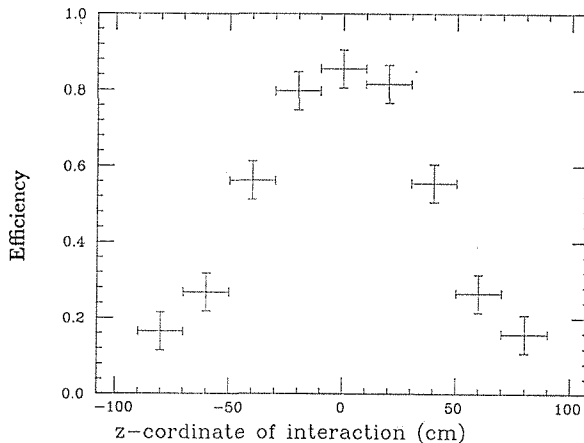

Fig. A-4. Hit efficiency of the inner chamber 'tower' for the beam-beam pipe interaction.

In this stage of the experiment at the beam energy of 26 GeV, the inner chamber was not fully operated due to heavy backgrounds from the beam pipe interaction. For this reason the inner chamber was not used for triggering, during the present measurement at 26 GeV.

References

(1–1) M. Kobayashi and T. Maskawa, Prog. Theor. Phys. **49** (1973) 652.
(1–2) J.J. Aubert *et al.*, Phys. Rev. Lett. **33** (1974) 1404;
       J.-E. Augustin *et al.*, Phys. Rev. Lett. **33** (1974) 1406;
       S.W. Herb *et al.*, Phys. Rev. Lett. **39** (1977) 252;
       PLUTO collab., Ch. Berger *et al.*, Phys. Lett. **76B** (1978) 243;
       DASP collab., C.W. Darden *et al.*, Phys. Lett. **76B** (1978) 246.
(1–3) UA1 Collab., G. Arnison *et al.*, Phys. Lett. **147B** (1984) 493.
(1–4) MARKJ Collab., D.P. Barber *et al.*, Phys. Lett. **85B** (1979) 463;
       PLUTO Collab., Ch. Berger *et al.*, Phys. Lett. **86B** (1979) 413;
       JADE Collab., W. Bartel *et al.*, Phys. Lett. **88B** (1979) 171;
       JADE Collab., W. Bartel *et al.*, Phys. Lett. **89B** (1979) 136;
       MARKJ Collab., D.P. Barber *et al.*, Phys. Rev. Lett. **44** (1980) 17
       PLUTO Collab., Ch. Berger *et al.*, Phys. Rev. Lett. **45** (1980) 153
       JADE Collab., W. Bartel *et al.*, Phys. Lett. **99B** (1981) 277;
       TASSO Collab., R. Brandelik *et al.*, Phys. Lett. **113B** (1982) 499
       MARKJ Collab., B. Adeva *et al.*, Phys. Rev. Lett. **50** (1983) 799;
       MARKJ Collab., B. Adeva *et al.*, Phys. Rev. Lett. **51** (1983) 443;
       TASSO Collab., M. Althoff *et al.*, Phys. Lett. **138B** (1984) 441;
       CELLO Collab., H.-J. Behrend *et al.*, Phys. Lett. **144B** (1984) 29
       TASSO Collab., M. Althoff *et al.*, Z. Phys. **C22** (1984) 307;
       MARKJ Collab., B. Adeva *et al.*, Phys. Lett. **152B** (1985) 439.
(1–5) MARKJ Collab., B. Adeva *et al.*, Phys. Rev. **D34** (1986) 681.
(1–6) JADE Collab., B. Naroska *et al.*, Phys. Rep. **148** (1987) 67.
(1–7) CELLO Collab., H.-J. Behrend *et al.*, Phys. Lett. **193B** (1987) 15
(2–1) TRISTAN project group, KEK Report 86–14, 1987.
(2–2) VENUS Collab., J. Iwahori *et al.*, KEK TRISTAN-EXP-001, 1983.
(2–3) Y. Yamada *et al.*, KUNS 853, 1986.
(2–4) R. Arai *et al.*, Nucl. Inst. Meth. **217** (1983) 181;
       F. Suekane *et al.*, IEEE Trans. on Nucl. Sci. **33** (1986) 73.
(2–5) Y. Hemmi *et al.*, Japan. Jounal of Appl. Phys. **26** (1987) 982;
       Y. Hemmi *et al.*, KUNS 835, 1986;
       Y. Yamada, Memoirs of the Faculty of Science, Kyoto University, Series of Physics, Astro-
           physics, Geophysics and Chemistry, Vol. **XXXVII**, No. 3, 1 (1989).
(2–6) R. Arai *et al.*, Nucl. Inst. Meth. **A254** (1987) 317.
(2–7) K. Ogawa *et al.*, Nucl. Inst. Meth. **A228** (1985) 309;
       K. Ogawa *et al.*, Nucl. Inst. Meth. **A243** (1986) 58;
       Y. Sumiyoshi *et al.*, KEK Preprint 87–120, 1987.
(2–8) H. Saito *et al.*, KEK Preprint 87–140, 1987.
(2–9) T. Uebayashi *et al.*, Nucl. Inst. Meth. **A265** (1988) 457.
(2–10) Y. Asano *et al.*, Nucl. Inst. Meth. **A259** (1987) 430;
       Y. Asano *et al.*, Nucl. Inst. Meth. **A259** (1987) 438.
(2–11) K. Amako *et al.*, KEK Preprint 87–153, 1988.
(4–1) B. Andersson *et al.*, Phys. Rep. **97** (1983) 33.
(4–2) CELLO Collab., H.J. Behrend *et al.*, Phys. Lett. **138B** (1984) 311
       JADE Collab., W. Bartel *et al.*, Z. Phys **C25** (1984) 231;
       MAC Collab. E. Fernandez *et al.*, Phys. Rev. **D31** (1985) 2724;

TPC Collab., H. Aihara *et al.*, Z. Phys **C28** (1985) 31.

(4–3) JADE Collab., W. Bartel *et al.*, Z. Phys **C33** (1986) 23.

(4–4) T. Sjostrand, Computer Phys. Comm. **39** (1986) 347;
       T. Sjostrand and M. Bengtsson, Computer Phys. Comm. **43** (1987) 3

(4–5) B.R. Webber, Nucl. Phys. **B238** (1984) 492.

(4–6) F. Berends *et al.*, Nucl. Phys. **B202** (1982) 63;
       F. Berends *et al.*, Computer Phys. Comm. **29** (1983) 185.

(4–7) MARKII Collab., A. Petersen *et al.*, Phys. Rev. **D37** (1988) 1.

(5–1) Y. Nakagawa *et al.*, Japan. Journal of Appl. Phys. **25** (1986) 104
       Y. Noguchi and A. Ono, Nucl. Inst. Meth. **A253** (1986) 27.

(5–2) VENUS collab. K. Abe *et al.*, J. Phys. Soc. Jpn. **56** (1987) 3767.

(5–3) E. Farhi, Phys. Rev. Lett. **39** (1977) 1587;
       A. De Rujula *et al.*, Nucl. Phys. **B138** (1978) 387.

(5–4) S. Brandl and H.D. Dahmen, Z. Phys. **C1** (1979) 61.

(5–5) J.D. Bjorken and S.J. Brodsky, Phys. Rev. **D1** (1970) 1416;
       G. Hanson *et al.*, Phys. Rev. Lett. **35** (1975) 1609.

(5–6) Particle Data Group, Phys. Lett. **170B** (1986) 1.

(5–7) S. Gusten *et al.*, Phys. Lett. **155B** (1985) 185.

(5–8) T. Sjostrand, Z. Phys. **C26** (1984) 93;
       JADE Collab., W. Bartel *et al.*, DESY 86–086 (1986).

(5–9) M. Bengtsson and T. Sjostrand, Phys. Lett. **185B** (1987) 435.

(A–1) J. Jersak *et al.*, Phys. Lett. **98B** (1981) 363;
       J. Jersak *et al.*, Phys. Rev. **D25** (1982) 1218.